HII and H2 in the envelopes of cooling flow central galaxies

Jaffe, W.J.; Bremer, M.N.; Baker, K.

Mon. Not. R. Astron. Soc. **360,** 748–762 (2005) doi:10.1111/j.1365-2966.2005.09073.x

H II and H_2 in the envelopes of cooling flow central galaxies

W. Jaffe,[1⋆] M. N. Bremer[2] and K. Baker[2]

[1] *Leiden Observatory, P.B. 9513, Leiden 2300 RA, the Netherlands*
[2] *Department of Physics, H. H. Wills Laboratory, Bristol University, Tyndall Avenue, Bristol BS8 1TL*

Accepted 2005 April 1. Received 2005 April 1; in original form 2005 January 18

ABSTRACT

We report observations of ionized and warm molecular gas in the extended regions of the central galaxies in several cooling flow clusters. These show that both gas phases are present in these clusters to large radii. We trace both Paα and H_2 lines to radii in excess of 20 kpc. The surface brightness profiles of the two phases trace each other closely. Apart from very close to the central active galactic nucleus (AGN), line ratios in and between the phases vary only slowly with position. The kinematics of the phases are indistinguishable, and away from the influence of the central AGN both the mean and dispersion in velocity are low ($\leqslant$100 km s^{-1}), ruling out kinematic support of the molecular gas. All of the above indicate that the mechanisms for heating the molecular gas and ionizing the H II regions are highly coupled. The highest surface brightness emission within a few kiloparsecs of the central AGN is distinct, both kinematically and thermally, from that at larger radii. The relative strengths of the Paα to the H_2 lines indicate a source of ultraviolet excitation rich in extreme-ultraviolet relative to far-ultraviolet photons, e.g. a blackbody with a temperature $\geqslant 10^5$ K.

Key words: molecular processes – H II regions – ISM: molecules – cooling flows.

1 INTRODUCTION

The density of the hot (10^7–10^8 K) intracluster medium (ICM) at the centres of many galaxy clusters is high enough for it to cool on time-scales less than the age of the cluster, potentially leading to the formation of a cooling flow (see Fabian 1994 for a review). Recent observations of galaxy clusters with *Chandra* and *XMM–Newton* have shown that the situation at the centres of clusters thought to contain cooling flows is considerably more complex than previously thought. *Chandra* and *XMM–Newton* data indicate that the size of a cooling region is typically smaller than was indicated by earlier *ROSAT* data (e.g. Peres et al. 1998), cooling may be intermittent, and there is considerable interaction between the hot phase at the centre of a cluster and any radio plasma emitted by the central radio source (Fabian et al. 2001; Böhringer 2001; McNamara et al. 2001). *Chandra* and *XMM–Newton* spectroscopy of the central regions of clusters reveals a lack of line emission expected from gas at ∼2 keV, implying that the amount of gas cooling through these temperatures is considerably less than the mass deposition rates determined from *ROSAT* data (e.g. see Peterson et al. 2003).

The existence of atomic and ionized gas emitting at 10^4 K in and around the dominant galaxies in many of these cooling flow clusters has been known for two decades (e.g. Hu et al. 1983; Heckman et al. 1989). Despite clearly being statistically correlated with the presence of the cooling flow in the cluster, the emission-line gas discovered in these early studies has too high a surface brightness and luminosity to be simple recombination radiation from material cooling through 10^4 K. It has long been recognized that this relatively high surface brightness emission must be excited by one or more mechanisms: hot stars, shocks, turbulence or X-ray heating.

Cooler molecular material associated with the optical nebulosity has recently been detected from its *K*-band H_2 line emission (Jaffe & Bremer 1997; Falcke et al. 1998; Wilman et al. 2000; Donahue et al. 2000). This material is dense ($n_e \geqslant 10^5$ cm^{-3}) and its occurrence correlates with that of atomic nebular emission (Jaffe, Bremer & van der Werf 2001). This, plus detection of large amounts of cold (<50 K) CO in cooling flows Edge (2001), indicates that large amounts of cool material are present at the centres of these clusters, even if the new X-ray data indicate weaker cooling than was previously estimated.

With the exception of the CO observations whose spatial resolution is so far quite poor, most previous studies of gas in brightest cluster galaxies (BCGs) have only detected gas within a few kiloparsecs of the nuclei, where the energetics of the gas are without doubt dominated by the activity of the active galactic nucleus (AGN), although Hatch et al. (2005) have detected molecular line emission in several star-forming regions at distances of $\gtrsim$25 kpc from the centre of the Perseus cluster. Our previous low resolution 4-m *K*-band spectroscopy has shown that there is a clear link between the intensities of emission lines from ionized and warm (∼2000 K) molecular gas at the centres of these clusters. We now extend this work by exploring the kinematic and morphological link between these two phases to larger radii (and lower surface brightness limits). This is

⋆E-mail: jaffe@strw.leidenuniv.nl

essential to separate the role of the AGN in these systems from that of the host galaxy and cooling flow in the excitation and dynamics of this gas.

With the goal of connecting the cooler intergalactic medium (IGM) states to that of the hot X-ray gas on scales of >10 kpc, we combine very deep narrow-band imaging of the BCGs of cooling flow clusters in the light of Hα λ6563 and [N II] λ6584 lines with deep 8-m long-slit *K*-band spectroscopy of a subset, obtained in order to examine the distribution and thermal state of the molecular gas through the 1–0 S and 2–1 S emission lines of H_2. The Paα emission in the *K*-band spectra allow us to link both data sets through comparison of the Hα and Paα lines.

2 OBSERVATIONS

2.1 Optical narrow-band imaging

The Hα + [N II] observations were performed at the Anglo-Australian Telescope (AAT) using the Taurus Tunable Filter (TTF) to obtain images with a bandwidth of ∼12 Å in all but one case. This Fabry–Perot etalon instrument, described in Bland-Hawthorn & Heath Jones (1998), has several advantages over conventional narrow-band imaging: very narrow bandpass, very short wavelength step between 'on' and 'off' bands, and *shuffling* between on and off images on the charge-coupled device (CCD) chip, which allows rapid switching between the two bands without increase in read-out noise. Together, these techniques yield images with very clean continuum subtraction, and independent maps of Hα and [N II].

The galaxies observed are given in Table 1. These include five strong cooling flow galaxies (as defined by the *ROSAT* observations, before *Chandra*/*XMM–Newton* re-observations), the non-cooling flow radio galaxy 3C 445 (a known line-emitting source at a similar redshift to the clusters) and the non-cooling flow cluster A3667. Here and further below, apparent quantities are converted to intrinsic quantities assuming $H_0 = 72$ km s^{-1} Mpc^{-1}, $\Omega_m = 0.3$ and $\Omega_\Lambda = 0.7$.

All clusters were observed with a bandwidth of 12 Å (full width at half-power, FWHP) except Abell 1795, which was observed with a bandwidth of 60 Å. Except for this cluster, each was observed at the redshifted wavelengths of Hα and [N II] (rest wavelength 6584 Å), although the [N II] image for Abell 2204 was corrupted and could not be reduced. Abell 1795 was observed with a single broader bandpass covering both lines. For our data, the etalon step between on- and off-line images was equivalent to approximately 40 Å blueward of Hα and 40 Å redward of [N II] (about twice this value for Abell 1795 because of its wider bandpass). The off-line image was sufficiently far removed in wavelength to avoid picking up any extended line emission present in any high-velocity wing of the emission line, but sufficiently close in wavelength that colour differences of the continuum between on and off bands will have a negligible effect on its removal from the on-line image.

Table 1. Clusters observed with TTF, with observed total fluxes and luminosities, or 3σ upper limits. Fluxes are in units of 10^{-15} erg s^{-1} cm^{-2}. Luminosities are in units of 10^{40} erg s^{-1}. All values are uncorrected for extinction.

Cluster	Redshift	*D* (Mpc)	Flux Hα	Flux [N II]	Luminosity Hα	Luminosity [N II]
3C 445	0.056	233	14.0	–	9.1	–
Abell 3667	0.056	232	<0.7	<0.7	<0.6	<0.6
Sersic 159-03	0.056	233	12.7	12.7	8.4	8.3
Abell 2029	0.076	316	<2.9	<1.4	<4.8	<2.3
Abell 2204	0.152	632	48.5	–[a]	232.7	–[a]
Abell 2597	0.082	343	41.5	28.7	80.7	55.7
Abell 1795	0.063	264	51.7[b]	N.A.	58.1[b]	N.A.

[a]The [N II] images of Abell 2204 were corrupted and could not be reduced.
[b]No independent [N II] measurement was taken for Abell 1795. The flux quoted for Hα includes the [N II] emission.

As expected from previously published less-sensitive observations, optical emission lines were detected from five of the sources. No significant emission was detected from Abell 2029 or the control cluster, Abell 3667. Grey-scale and contour plots of the detected clusters are shown in the left and centre panels of Figs 1–5 and for four clusters the contour plots are overlaid on *Chandra* X-ray images in the right-hand panel. These images were extracted from the *Chandra* science archive site.[1] They represent data from the ACIS-S3 chip, summed over the 0.3–7.0 keV energy range, and reduced with the CIAO 3.0 software package. The photon counts were smoothed with a 4.4 arcsec full width at half-maximum (FWHM) Gaussian kernel. The log of the *Chandra* observations is given in Table 2.

In Table 1 we also list the integrated fluxes and luminosities contained within a perimeter drawn at a level equal to the rms noise in the image. In Figs 6 and 7 we plot the azimuthally averaged surface brightness of the emission lines in each of the four well-resolved sources as a function of radius from the galactic nucleus.

2.2 *K*-band spectroscopy

In order to probe in detail the connection between the atomic and molecular phases of the line-emitting gas, we obtained medium-resolution spectroscopy of a subset of the above cluster sample. These observations were obtained with ISAAC on the Very Large Telescope (VLT). The sample was that subset of the optical imaging sample described above, showing emission at large radii and easily visible from the Southern hemisphere. Figs 1, 2 and 4 show the positions of the slits superimposed on the contour maps obtained in the previous section.

Because of the extended nature of the Hα emission, we used a relatively wide slit (1 arcsec) for the infrared (IR) spectroscopy, assuming (correctly) that the IR lines would be similarly extended. The slit was generally oriented through the galaxy nucleus and at a position angle at which we had previously observed extended Hα emission. We used the ISAAC medium-resolution (MR) grating, with a resolution of ∼3000, after experience showed that the results with the low-resolution (LR) grating ($R \sim 500$) were inferior. The main advantage of the MR system is that the *K* band contains several strong telluric absorption systems near the 2-μm end of the band and with the LR system the individual lines in these systems blend together. This makes it difficult to detect weak extraterrestrial emission in this region. With the MR system the individual lines are separated, and emission can easily be detected between the absorption lines.

A disadvantage of this approach is that we cannot observe the entire *K* band in one setting of the spectroscope. The observable band was about 0.12 μm at any one setting of the central wavelength. We have chosen to take one spectrum in the vicinity of Paα, H_2 1–0 S(3) (and occasionally other lines), and one in the vicinity of H_2 1–0 S(1). Because of variations of the exact bandpass with redshift,

[1] http://asc.harvard.edu/targets

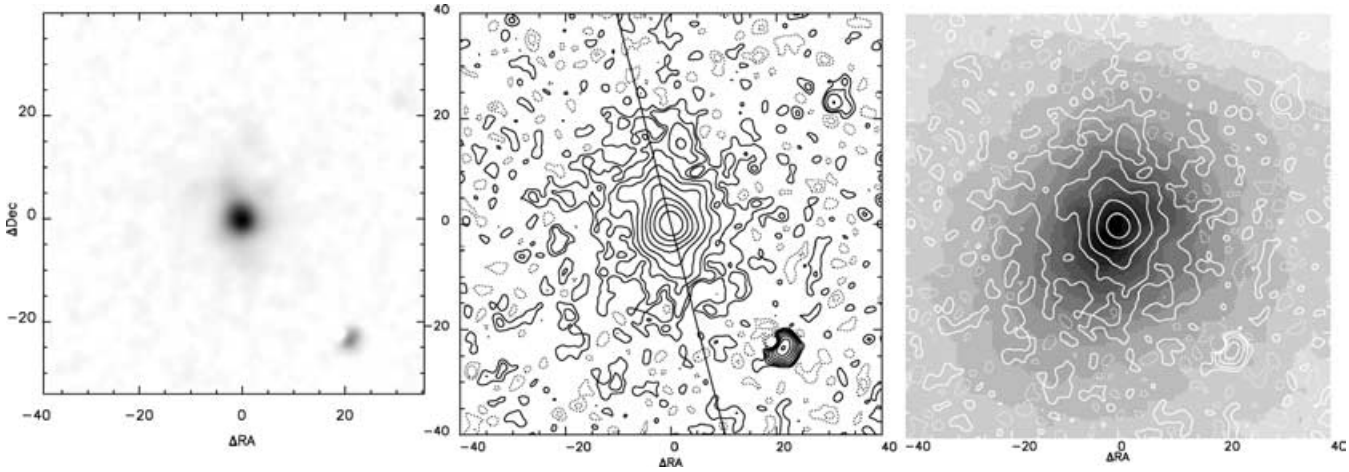

Figure 1. Images of the line emission around A2597. North is up and east at the left. Coordinates give the offsets from the nucleus in arcsec on the sky. At Abell 2597, 1 arcsec = 1.66 kpc. The small feature in the bottom right is the residual image of a bright star. Grey-scale (left) and contour (middle) plot of Hα + [N II]. Lowest solid contour is at 3.0×10^{-18} erg s^{-1} cm^{-2} arcsec^{-2}. In this and following figures, the subsequent contours double in surface brightness, while dashed contours represent negative (noise) values. Contour plot (right) of line emission overlaid on grey-scale of *Chandra* X-ray emission from cluster. For clarity in the overlay, every other contour has been omitted.

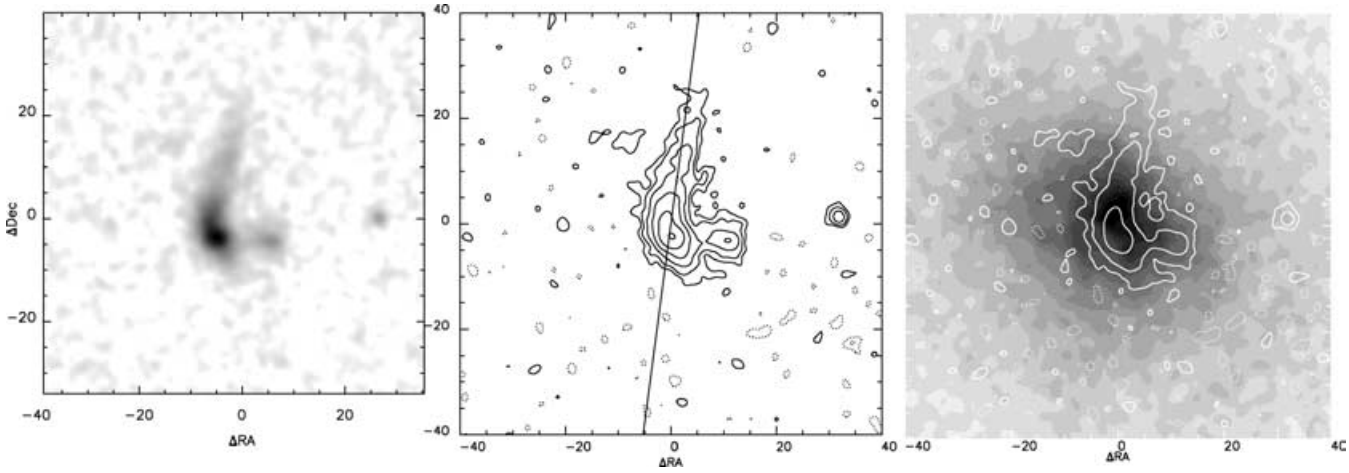

Figure 2. Images of the line emission around Sersic 159-03; 1 arcsec = 1.13 kpc. Grey-scale (left) and contour (middle) plot of Hα + [N II]. Lowest contour is at 3.0×10^{-18} erg s^{-1} cm^{-2} arcsec^{-2}. Contour plot (right) overlaid on *Chandra* image.

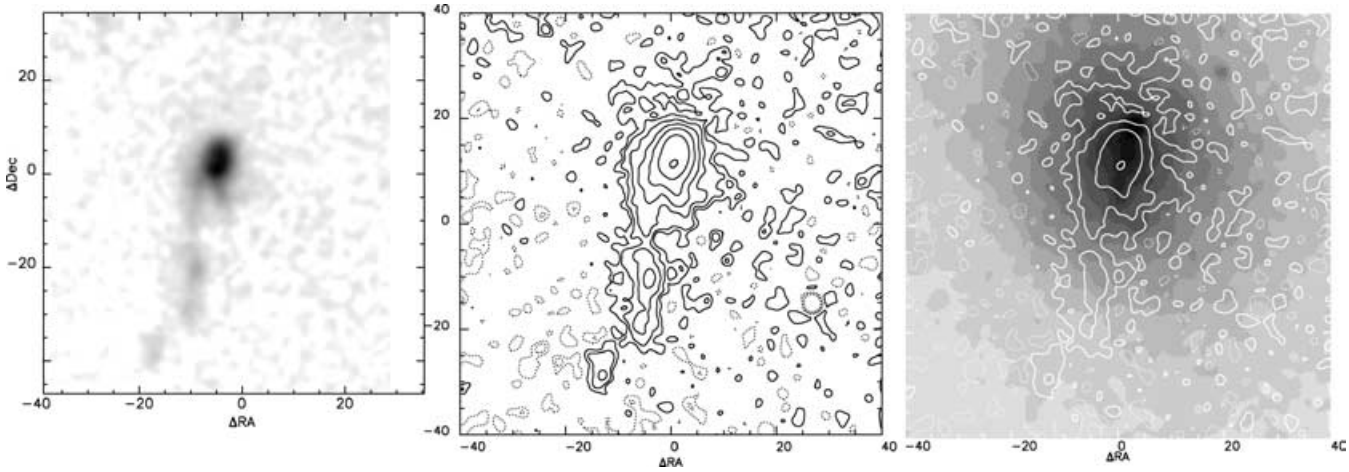

Figure 3. Images of the line emission around Abell 1795; 1 arcsec = 1.27 kpc. Grey-scale (left) and contour (middle) plot of Hα + [N II]. Lowest contour is at 4.6×10^{-18} erg s^{-1} cm^{-2} arcsec^{-2}. Contour plot (right) overlaid on *Chandra* image.

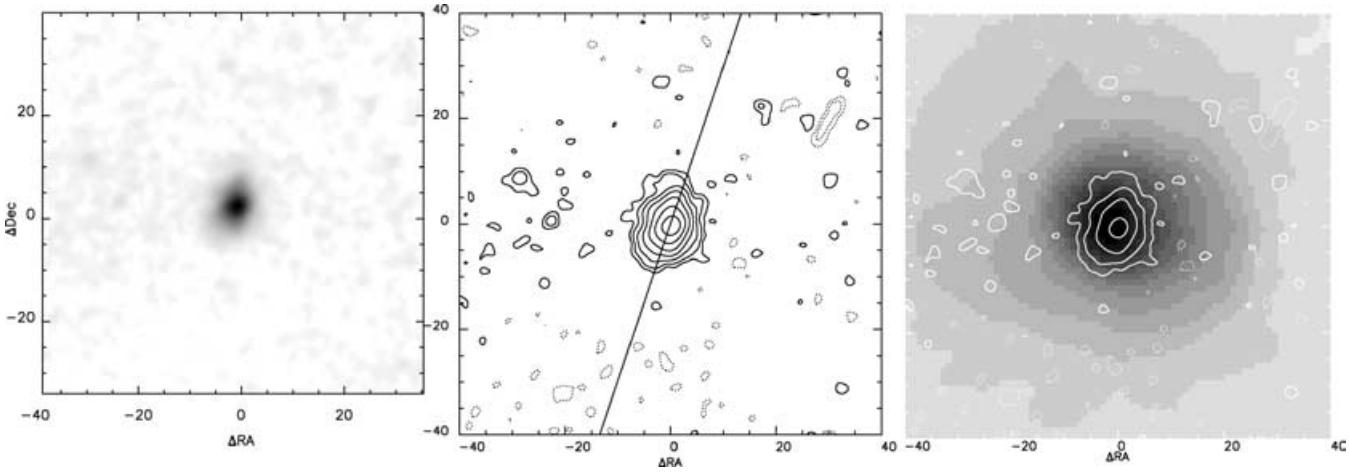

Figure 4. Images of the line emission around Abell 2204; 1 arcsec = 3.2 kpc. Grey-scale (left) and contour (middle) plot of Hα only. Lowest contour is at 1.3 $\times$ 10^{-17} erg s^{-1} cm^{-2} arcsec^{-2}. Contour plot (right) overlaid on *Chandra* image.

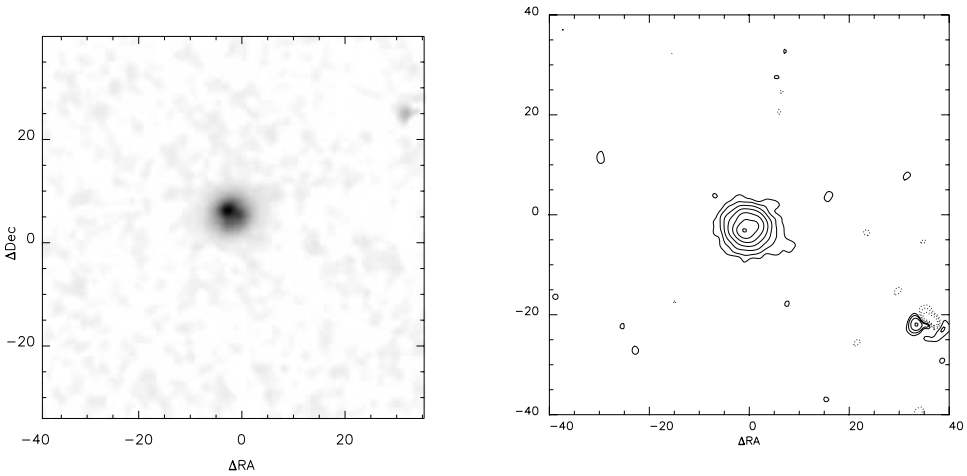

Figure 5. Contour plot of 3C 445 Hα emission; 1 arcsec = 1.13 kpc. Lowest contour is at 5.25 $\times$ 10^{-18} erg s^{-1} cm^{-2} arcsec^{-2}.

Table 2. Observing log of clusters observed with *Chandra*.

Cluster	Exposure time (ks)	Observation date
Abell 1795	20	2000 March 21
Abell 2204	30	2000 July 29
Abell 2597	40	2000 July 28
Sersic 159-03	10	2001 July 13

and small errors in redshift, some of the less important lines at the edges of the spectra (e.g. Brγ) were not observed for all clusters.

Standard stars, usually B stars of magnitude $K \sim 7$, were observed to correct for telluric absorption and to provide calibratable fluxes. These standard spectra were used to remove the continuum emission by a linear fit to the galactic emission in regions where no galactic emission or absorption lines are expected. Additional smooth power-law components are also removed, which mostly reflect the difference in blackbody slope between the galactic stars (mostly *K* and *M* giants) and the standards. Any absorption lines in the standard stars then remain as emission lines in the final spectra. This is sometimes a problem near rest wavelength Brγ. The aforementioned spectral mismatches appear mostly as very weak absorption or emission features, before correcting for the total telluric absorption.

These 'raw' two-dimensional spectra are shown in Figs 8–10. In these 2D spectra we see the gaseous emission lines, along with noisy vertical stripes at wavelengths of high telluric absorption. By Kirchhoff's principle, the atmospheric thermal emission at these wavelengths is maximum. The photon noise from the atmospheric emission is the chief source of noise in the final spectra, and thus maximum at the position of the absorption lines. At the *y*-position of the maximum of the galactic continuum we also see small features due to minor stellar absorption/emission mismatches between target galaxy and standards.

3 DISCUSSION

3.1 Extent, morphology and kinematics of the 'warm' gas phases

Figs 1–5 show that the warm H II phase ($T \sim 10\,000$ K) can be traced to radii beyond 20 kpc in all four cooling flows. In Abell 2204 we see emission to 30 kpc and in Abell 2597 to beyond 40 kpc in smoothed

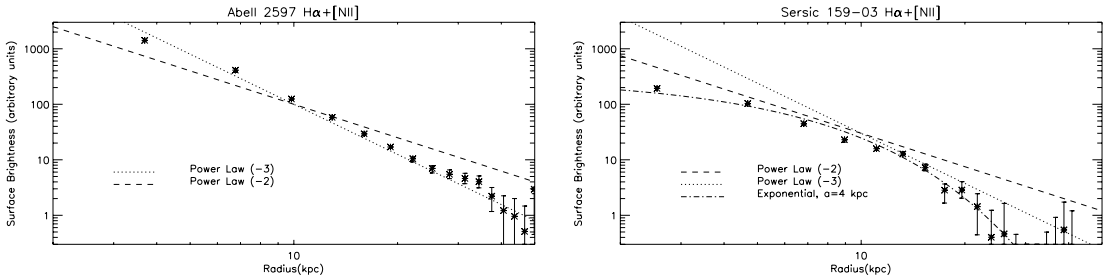

Figure 6. Averaged surface brightness in combined Hα and [N II] emission in circular annuli around the nucleus of Abell 2597 (left) and Sersic 159-03 (right). The error bars include noise, intrinsic non-circularity and estimates of the uncertainty in the background subtraction at large radii. For radii less than $\sim$15 kpc the error bars are smaller than the plotting symbols. Also shown are power-law curves for r^{-2} and r^{-3} laws and for Sersic 159-03 an exponential curve $\Sigma \propto \exp(-r/a)$.

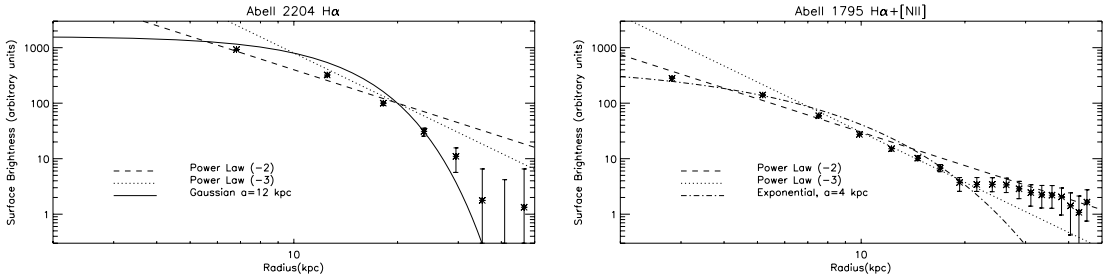

Figure 7. Averaged surface brightness in circular annuli around the nucleus of Hα in Abell 2204 (left) and Hα combined with [N II] in Abell 1795 (right). Also shown are power laws, for Abell 2204 a Gaussian relation $\Sigma \propto \exp(-r/a)^2$, and for Abell 1795 an exponential relation.

images. This last figure can be compared to the H II structure seen in the same cluster to about 20 kpc in Heckman et al. (1989) and the bright central features associated with the central radio source at $\sim$5 kpc shown in Koekemoer et al. (1999). The increased maximum radius of detection for this source corresponds to an increase in surface brightness sensitivity by a factor of 20 relative to Heckman et al. (1989).

The four clusters have diverse morphologies: extended and roughly circularly symmetric (Abell 2597), compact (Abell 2204), and arc-like (Abell 1795 and Sersic 159-03). Ignoring these differences, we have plotted the radial surface brightness distribution, averaged over annuli centred on the galaxy nucleus in Figs 6 and 7. The averaging over a large number of pixels at larger radii improves the signal-to-noise ratio at these radii.

Abell 2597 shows significant emission, distributed essentially as an r^{-3} power law to beyond 40 kpc, where it disappears smoothly into the noise. The 'arc-like' structure of Abell 1795, when azimuthally averaged, shows similar behaviour, with perhaps a slightly flatter distribution with radius ($\propto r^{-2}$). Abell 2204 shows emission to a similarly large radius ($\sim$35 kpc) but drops more rapidly than a power law, more like a Gaussian, with a radius of $\sim$12 kpc. In other words, the apparent size of the emission region seems to be a real physical characteristic of the source, rather than a limit imposed by our surface brightness sensitivity. In Sersic 159-03 the circularly averaged emission can be traced to radii just beyond 20 kpc and is fitted approximately by an exponential with scale sizes of $\sim$4 kpc. Thus the increased sensitivity afforded by the TTF system yields two contrasting results: in Abell 2597 and 1795 we can trace the smooth decrease in surface brightness to double the previous limiting radius but find no physical edge; in the other two clusters we can establish the existence of a radius characteristic of the source physics.

Figs 8–10 show strikingly that molecular emission can be traced to $\sim$25 kpc and that the Paα and H_2 line profiles are virtually indistinguishable both spatially and kinematically. A comparison of the Paα lines and the 1–0 S(1) and 1–0 S(3) lines shows that, taking differing signal-to-noise ratios and interfering sky lines into account, every feature visible in one line is visible in the others at the same velocity and position and essentially the same intensity. This implies directly that the H II and warm H_2 gas phases and their respective excitation sources must be well mixed on scale sizes finer than 1 kpc, and the relative mix is essentially constant over factors of 10 in radius. The correspondence suggests further that the H_2 phase is present wherever the diffuse H II can be observed, i.e. to beyond 40 kpc in Abell 2597.

Consistent with our earlier work, the ratio of H_2 to H II linestrengths is far higher than that found in typical galactic star-forming regions and starburst galaxies (by H II lines, we mean hydrogen recombination lines from the Balmer and Paschen series, arising in H II regions). In fact, the combined luminosity in all the near-infrared (NIR) H_2 lines is comparable to that in all the optical H II lines, although the luminosity in Lyα is probably an order of magnitude above this.

The velocity structure of the molecular gas in all three observed clusters shows a division into two regions: a central area of radius $\sim$5 kpc with high velocity dispersion, and a larger region of 5–25 kpc with much lower dispersion. The one-dimensional spectra presented in previous works including our own are dominated by emission from this central region.

In this region, where the gas is probably stirred by the AGN, the velocity spreads – here quoted as the line-of-sight rms velocity dispersion σ – range from $\sim$120 km s^{-1} for Sersic 159-03 through 200 km s^{-1} for Abell 2597 to 300 km s^{-1} for Abell 2204. The areas at larger radii show lower dispersion ($\lesssim$60 km s^{-1}) and apparent

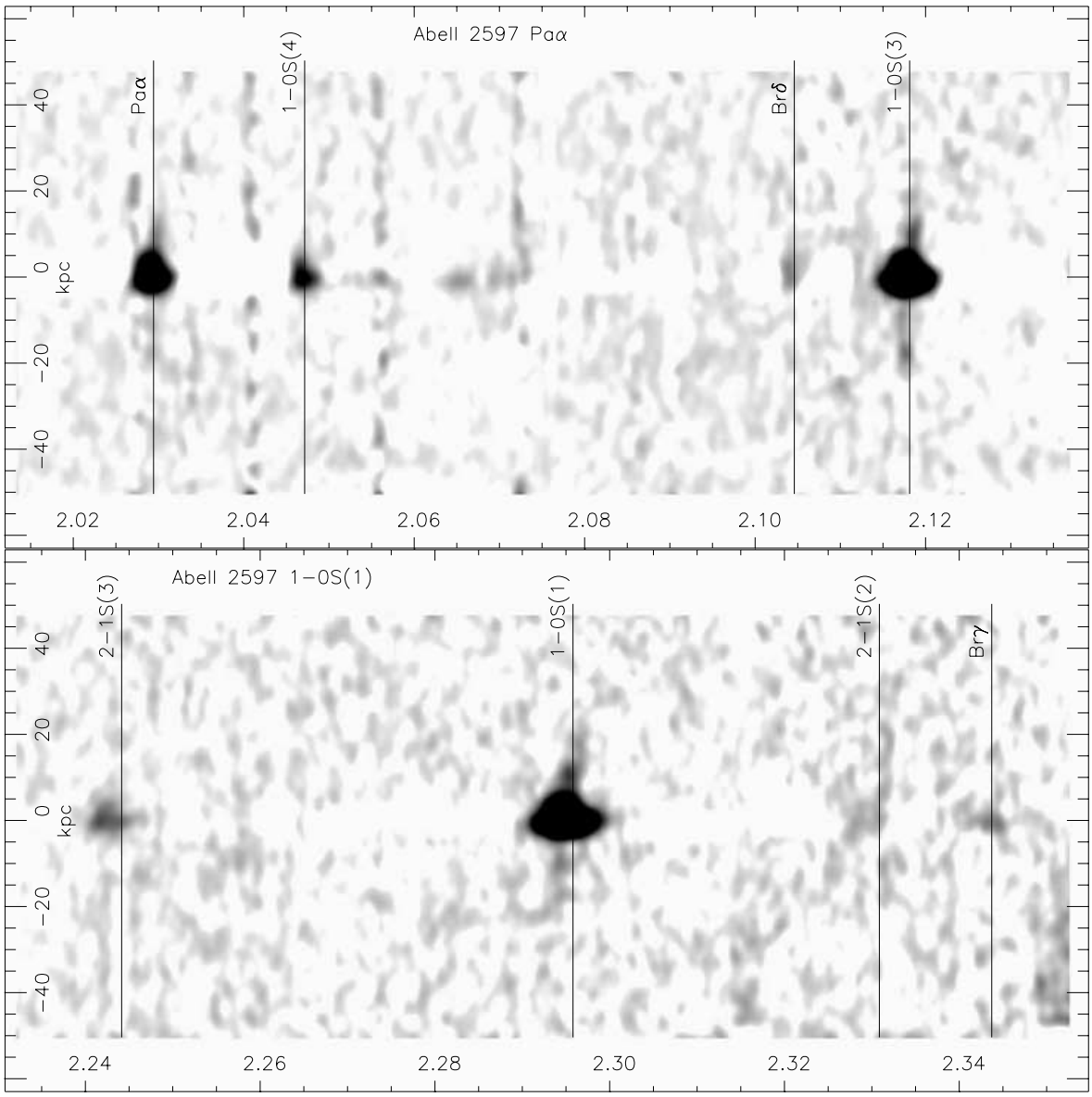

Figure 8. Raw two-dimensional spectra of Abell 2597 in the regions of Paα and 1–0 S(1), respectively. The abscissa gives the laboratory wavelength in micrometres.

large-scale rotation or shear motions of magnitude $\sim$100 km s^{-1}. These dispersion estimates are in fact upper limits set by the velocity resolution of our wide-slit spectroscopy and the true values could be lower. For Abell 2204 and 2597, Edge (2001) finds linewidths in the CO molecular emission of 255 and 278 km s^{-1}, respectively, with a beam size of 22 arcsec. These values seem lower than we would expect from our K-band data, given that our central FWHP 'widths' are 700 and 470 km s^{-1} for these two clusters, and that the K-band line emission is strongly peaked towards the centres. This would indicate that the cold molecular gas responsible for the CO emission does not partake of the violent motions near the galaxy centre and is situated at radii beyond $\sim$10 kpc.

At the larger radii the gas velocity dispersions and rotational velocities are much smaller than the typical stellar dispersion velocities in BCGs: 400–600 km s^{-1}. Thus the molecular gas clouds at large radii *are not kinematically supported* nor, given their high density, can they be supported by pressure gradients in the surrounding hot gas. The low velocities that we see are dynamically consistent only if this gas has been formed from a pressure-supported phase in the last 10^7 yr (the time necessary for gravity to accelerate them to above 100 km s^{-1}) or if an as yet unknown mechanism supports them. Daines, Fabian & Thomas (1994) have suggested magnetic support of the clouds. This seems unlikely to us, however, because of the Parker instability (Parker 1968) generally present in gas supported against gravity by magnetic fields.

From our Hα fluxes, with corrections for dust absorption (see below), we can calculate the total mass of warm ionized gas in the cluster centres. Because of the relatively fast drop of brightness with radius, we do not, however, expect these estimates to be much larger than older data obtained at higher surface brightness limits.

For Abell 2597, assuming $n_e \sim 200$ cm^{-3} (Heckman et al. 1989) and $A_{H\alpha} \sim 1$, we find an H II mass of $\sim 3 \times 10^7\,M_\odot$. The mass in *warm* H_2 can be estimated from $M_{H_2} = 2\,m_H L_1/(\epsilon_1 A_1 F_1)$, where L_1 is the luminosity in the 1–0 S(1) line, ϵ_1 is the energy of the

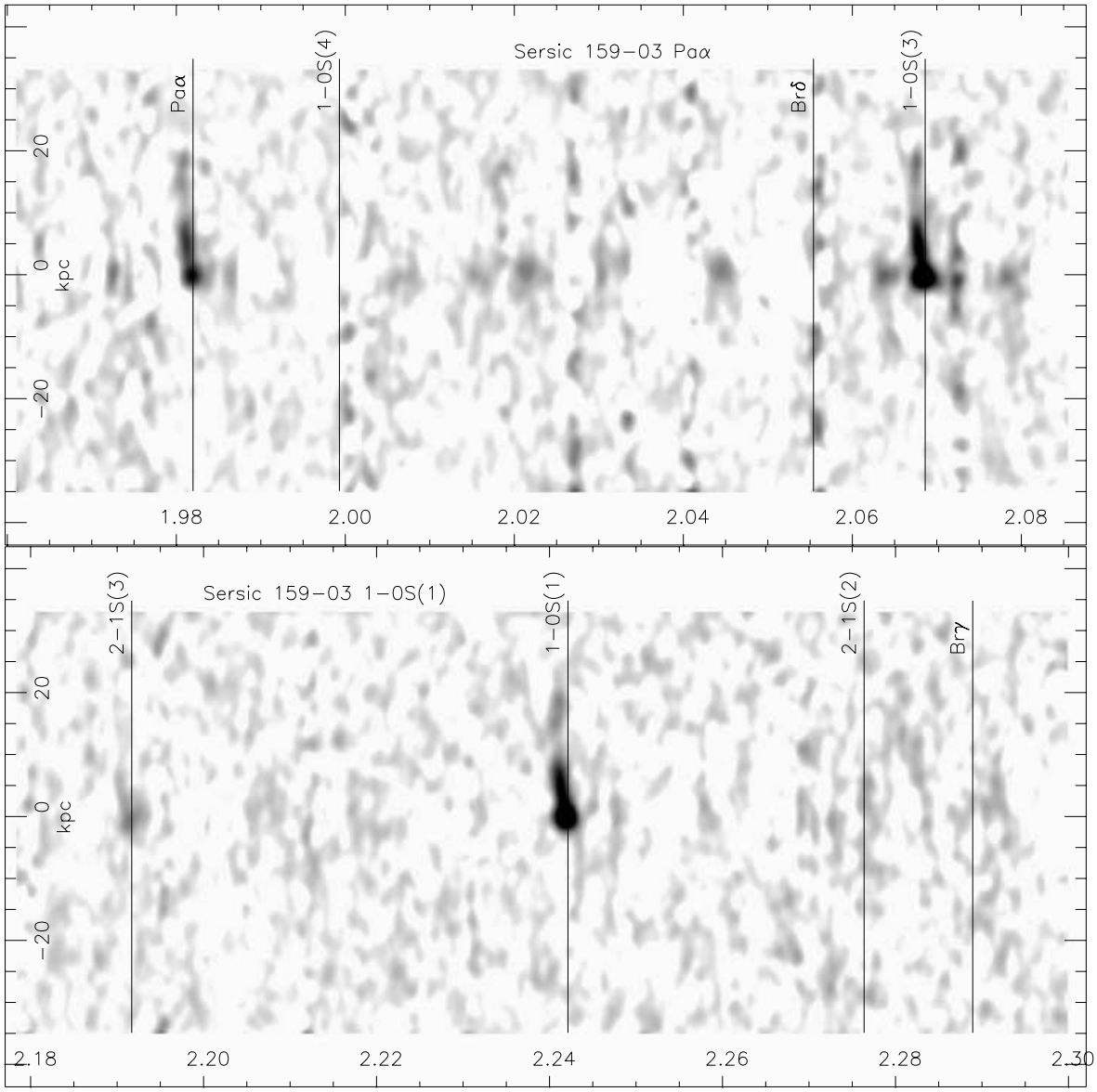

Figure 9. Raw two-dimensional spectra of Sersic 159-03 in the regions of Paα and 1–0 S(1), respectively.

photon from this transition, A_1 is the Einstein coefficient for this transition, and F_1 is the fraction of all H_2 molecules to be found in the upper state for this line. For local thermodynamic equilibrium (LTE) conditions at $T \sim 2000$ K (cf. Section 3.2.4), F_1 is ∼0.015. With the assumption that the ratios of 1–0 S(1) to Paα and Paα to Hα vary globally in the same way as they do along our slit measurements, we find $L_1 \sim 10^{42}$ erg s^{-1} for both Abell 2597 and 2204, with a corresponding M_{H_2} of $\sim 4 \times 10^5$ M$_\odot$. This is much smaller than the masses of *cold* H_2 found by Edge (2001) to be $\sim 10^9$–10^{10} M$_\odot$. The H_2 masses calculated in that article are based on 'standard' ratios of H_2/CO, and Israel (1997) shows that these may in fact be serious underestimates in cases where the molecular gas is exposed to a bright ultraviolet/X-ray radiation field, which dissociates the CO molecule. The kinetic energy in the warm molecular gas in the 'violent' central region is of the order of 10^{54} erg and, if it is dissipated in the central dynamic time of $\sim 2 \times 10^7$ yr, the corresponding kinetic luminosity is of the order of 10^{39} erg s^{-1}, which is small relative to other luminosities associated with the AGN and cooling flow. If, contrary to our inference above, the cold gas also partakes of this rapid turbulent motion, its kinetic luminosity would of course be much larger and would become important to the energetics of the system as a whole.

The problem of the support of the molecular gas takes on its most serious form for the cold 'CO' gas. The gravitational potential energy of this gas, $\Phi_{\rm cold}$, can be estimated as $M_{\rm cold}\sigma_*^2$, where σ_* is the three-dimensional velocity dispersion of the stars (∼600 km s^{-1}); $\phi_{\rm cold} \sim 3 \times 10^{58}$ erg. This is the same order of magnitude as the *total* thermal energy of the X-ray gas within 15 kpc of the galaxy centre (Kaastra et al. 2004) and similarly the entire magnetic energy in this region, assuming $B \sim 10\,\mu$G (e.g. Taylor, Fabian & Allen 2002).

3.2 Line ratios and thermal structure of the warm gas phases

Figs 8–13 illustrate the similarity of the surface brightness profiles for the NIR H II and H_2 lines. To allow a more direct comparison

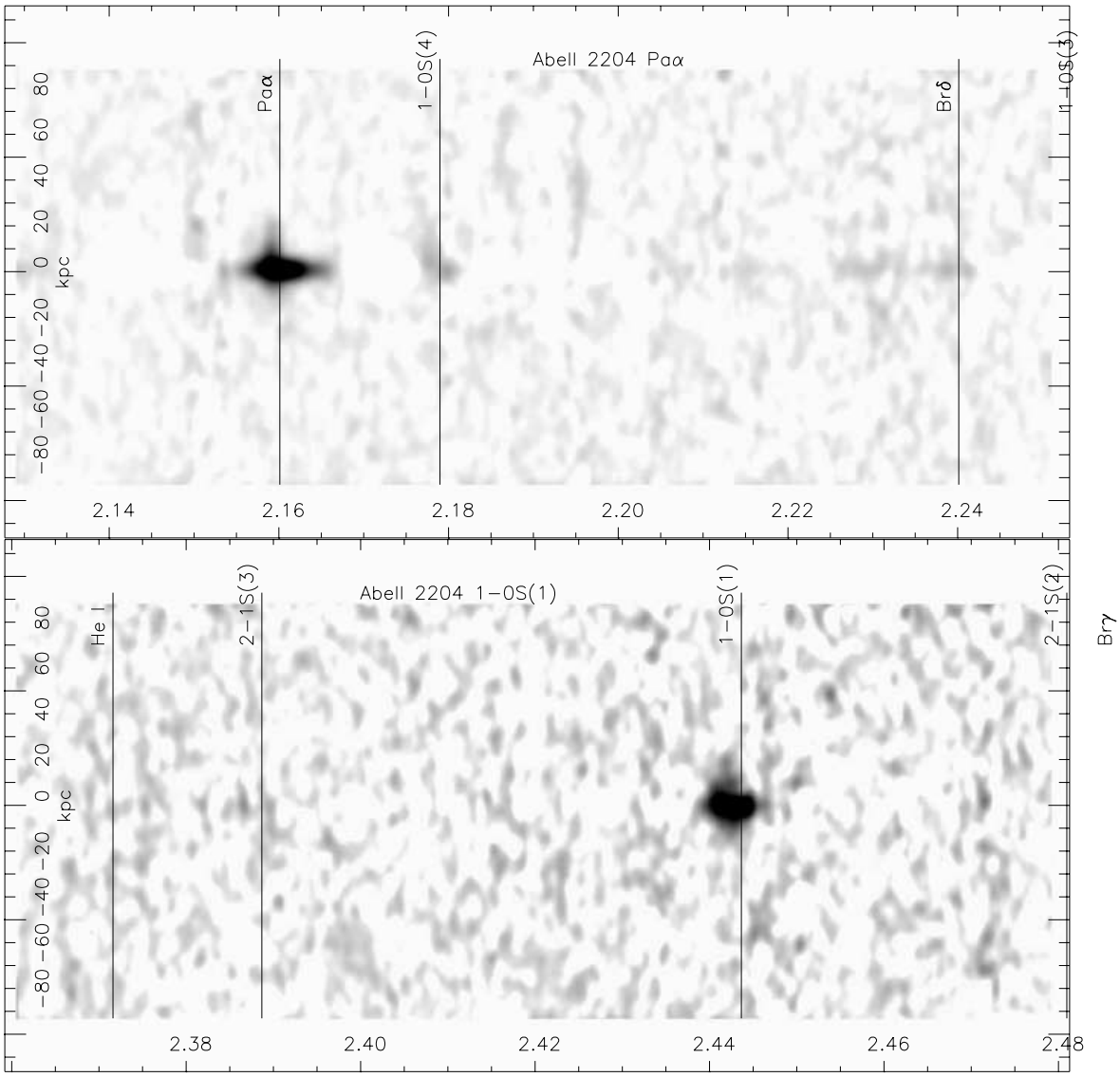

Figure 10. Raw two-dimensional spectra of Abell 2204 in the regions of Paα and 1–0 S(1), respectively.

of the line ratios of the strongest lines [1–0 S(1), 1–0 S(3) and Paα], we have integrated them in velocity and plotted them as a function of slit position in the third panels of Figs 14–16. In each case, the spectra have been plotted on a logarithmic intensity scale, and scaled to the flux of 1–0 S(1) at the centre. In the fourth panel of these figures, we have plotted in a similar fashion the intensities of Hα, [N II] and Paα, where the *optical* lines have been evaluated from the TTF images along the position of the NIR slit. In estimating the absolute IR/optical ratios, some uncertainties in this procedure are inevitable: the different observing and calibration techniques may introduce errors of ∼30 per cent, and errors in the exact alignment of the slit on the images may be of the order of 1 arcsec. Experiments with moving the positions or position angles of the slit on the image did not produce significant changes in the shapes of these plots. Additionally, the narrow bandpass (12 Å) of the TTF filters will miss some optical flux at the central high velocity width position. Assuming a Gaussian profile with the dispersions plotted in the figures, we find that about 40 per cent of the Hα flux at the centre of Abell 2204 would be lost ($\sigma = 300\,\mathrm{km\,s^{-1}}$), 20 per cent at the centre of Abell 2597 ($\sigma = 200\,\mathrm{km\,s^{-1}}$), and a negligible loss in Sersic 159-03.

3.2.1 *Dust extinction*

Under the assumption of Case-B ionization equilibrium in the H II regions, the Pα/Hα ratio is ∼0.12 (Osterbrock 1974). All three of the objects with ISAAC spectra show larger ratios at the peak of their surface brightness profiles: 0.76 for Abell 2597, 0.55 for Sersic 159-03, and 0.24 for Abell 2204. For the first two clusters this implies extinction of $A_{\mathrm{H}\alpha} \sim 1.6$–$1.8$ mag, with calibration uncertainties of ∼0.5 mag, and reddening of $E(B-V) \sim 0.6$. For Abell 2204, after correction for Hα lost outside the filter bandpass, the estimated extinction is small, <1 mag. In determining these numbers, we have assumed that the dust is in a screen in front of the gas, whereas in reality the dust could well be mixed in. Nevertheless, the numbers give an indication of the amount of dust in or around the emission-line regions.

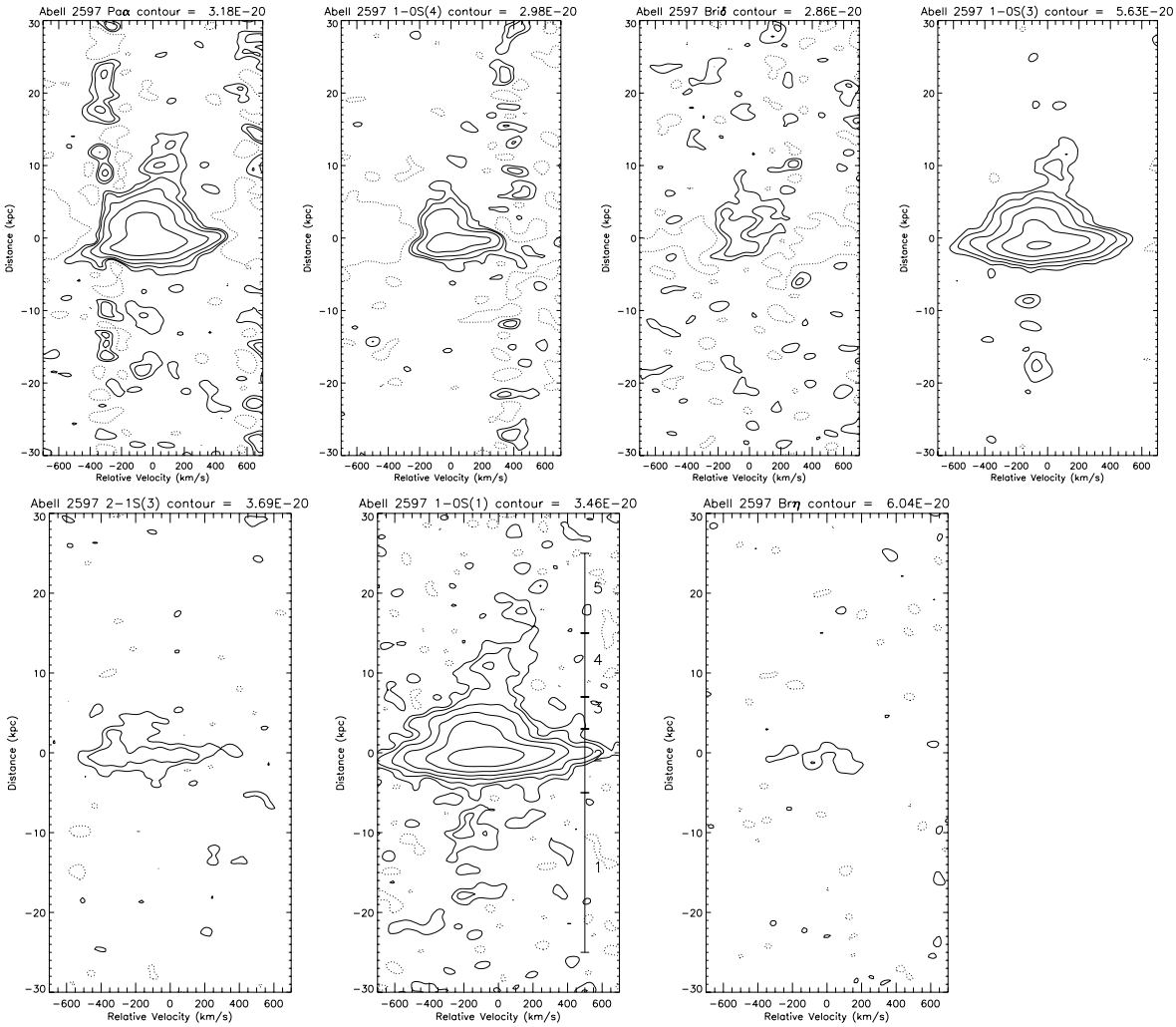

Figure 11. Contour maps of calibrated stronger detected lines in Abell 2597. Contours are [−1, 1, 2, 4, 8, 16, . . .] times the lowest level (in erg s^{-1} cm^{-2} $arcsec^{-2}$), which is indicated in the figure title. The vertical bar in the 1–0 S(1) map marks the regions for which LTE line ratio plots are given in Fig. 18.

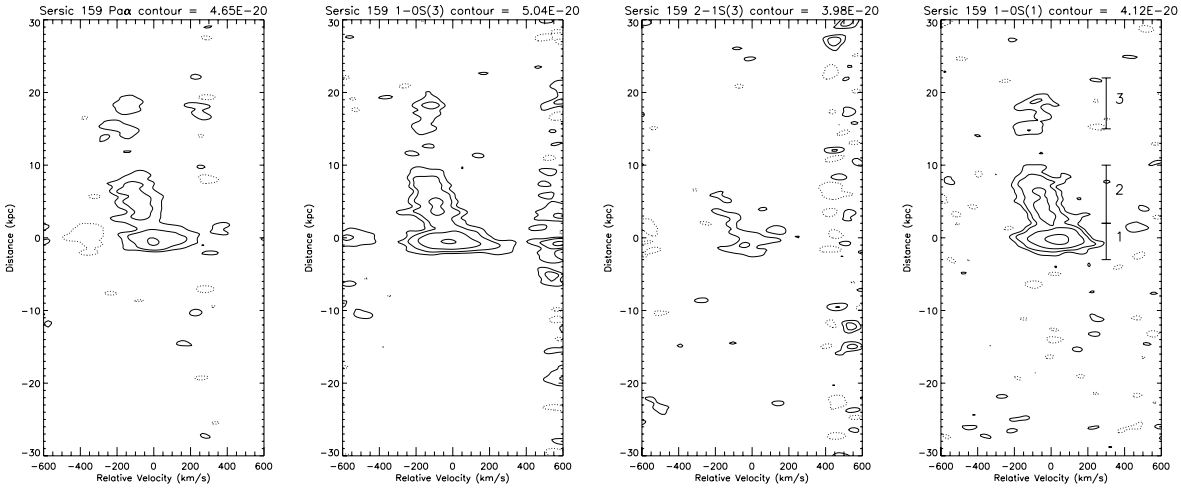

Figure 12. Contour maps of calibrated stronger detected lines in Sersic 159-03.

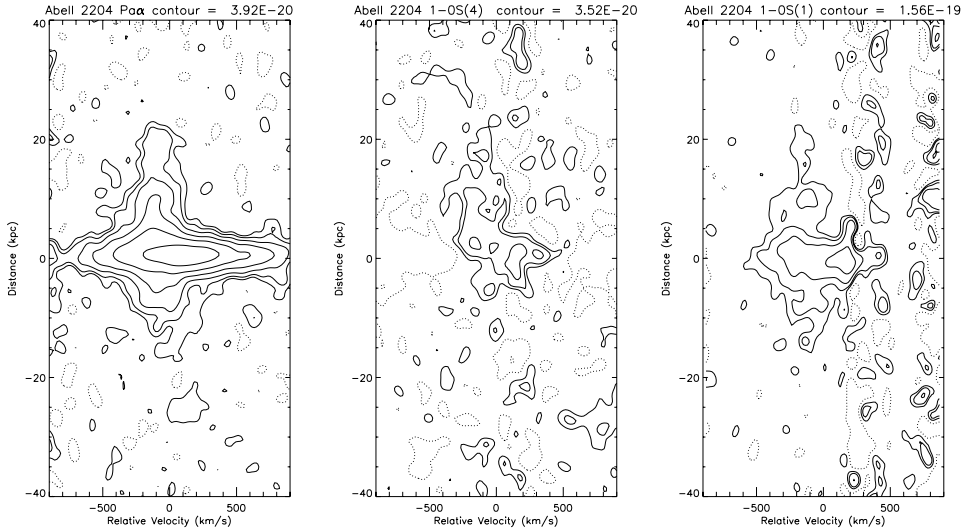

Figure 13. Contour maps of calibrated stronger detected lines in Abell 2204.

In the case of Abell 2597, this ratio decreases smoothly by a factor of 2–3 as r increases to ± 15 kpc from the centre of the nebulosity, corresponding to a drop in extinction to $\sim$1 mag. We see a similar trend for Abell 2204 probably due to a reduction in loss outside the Hα filter, i.e. showing little evidence for extinction at any radius.

The situation is more complicated for Sersic 159-03. Along the 'tail' of emission north of the peak surface brightness, the line ratio barely varies significantly; possibly the Pα/Hα ratio increases slightly relative to the peak, implying an increase of 0.2–0.3 in $E(B-V)$ at most. To the south, the surface brightness drops sharply. Although Fig. 15(d) shows a sharper drop in Paα than Hα, indicating a decrease in reddening, differences in the seeing and pixel size between the two data sets may cause this. These systematic effects limit our ability to draw firm conclusions about the effect of reddening in this region.

What is clear from the above is that many line-emitting clouds up to 20 kpc from the centres of these clusters contain dust, and the reddening effect of the dust does not vary dramatically across the nebulosity, apart from at their very centres. Koekemoer et al. (1999) have already shown that there is a probable dust lane crossing the nucleus of Abell 2597; this is the obvious explanation for the excess reddening we see at the centre for this source.

3.2.2 *[N II]/Hα line ratios*

The ratio of the forbidden [N II] line to the permitted Hα line can be taken as a crude measure of ionization parameter $\Xi \equiv n_{\rm photon}/n_{\rm H}$; larger values of [N II]/Hα correspond to larger values of Ξ. Heckman et al. (1989) have shown that, from cluster to cluster, various ionization measures correlate with each other, and that ionization correlates inversely with Hα luminosity. Crawford & Fabian (1992) and Crawford et al. (1995, 1999) have shown that these correlations are quite general in cooling flows, but that the line ratios vary continuously rather than forming two distinct classes as claimed by Heckman et al. (1989). For the two clusters where we have good TTF maps of these lines, the line ratios are displayed in Fig. 17.

We find that, between these two clusters, the relation between [N II]/Hα varies in the sense described in the quoted papers, but that locally, within each cluster, this is not true, and that the two clusters appear quite different. In Abell 2597 there is a some tendency for this ratio to increase where the surface brightness of Hα decreases, but the effect is only strong at the very edges of the nebulae. Log([N II]/Hα) is in fact very nearly constant at a low value ~ -0.2 typical of the high-luminosity 'Type II' of Heckman et al. (1989) along a north-east to south-west (NE–SW) axis, more or less parallel with the radio jet axis, rising to the 'Type I' value of $\sim +0.3$ on the NW and SE perimeters. The source average is dominated by the central, lower value. Sersic 159-03 shows the opposite behaviour: the brighter central regions show a high value of log([N II]/Hα), while the perimeter shows lower values; the high value dominates the average.

We note that the ionization level is not simply related to distance from the galactic nucleus. In Abell 2597 the line ratio varies little when the radius varies by a factor of more than 10. This fact emphasizes, as other authors have noted, that the source of excitation is almost certainly not the AGN but rather has an origin local to the ionized gas. The difference between the two clusters emphasizes that the interpretation of these line ratios is not simple, as they depend on metallicity, ionization parameter and density.

3.2.3 *Comparison between H_2 lines and Paα*

Using our ISAAC spectroscopy, we are able to compare the spatially resolved properties of the Pα and H_2 1–0 lines. Previous work has concentrated on the integrated properties of the highest surface brightness IR lines. These spectra are invariably dominated by emission from the very centres of the galaxies (which harbour strong radio sources) and likely to be influenced by the effect of AGN emission.

We can compare three main spatially varying parameters of the lines: their surface brightness profiles, their velocity dispersions and their peculiar velocities relative to the centre of the galaxy. Figs 6–14 show that the atomic and molecular hydrogen lines behave very similarly as a function of position.

The velocity structure in all the lines looks similar. As noted in Section 3.1, the central high surface brightness regions have velocity dispersions of several hundred km s^{-1}, while at larger radii the dispersion in all lines drops to approximately 60 km s^{-1}, the resolution of the spectrograph, and probably lower. The molecular and atomic lines show similar variations in peculiar velocity as

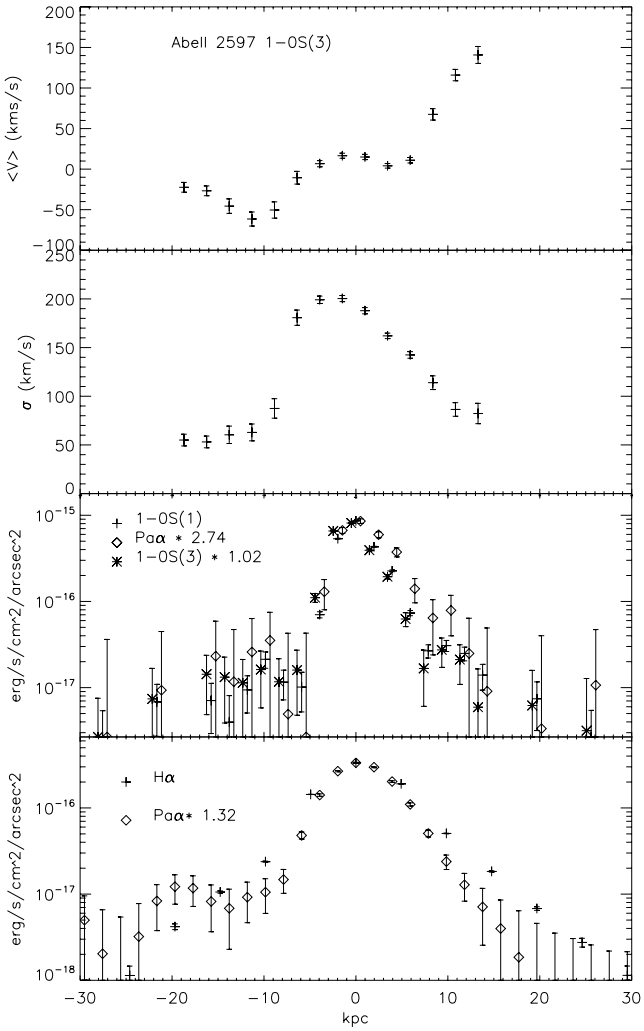

Figure 14. Abell 2597 spectral data as a function of distance along the slit. The top and second panels give mean velocity and velocity dispersion taken from the 1–0 S(3) line. The third panel gives the surface brightness of the IR lines. The ordinate gives the surface brightness of the 1–0 S(1) line. The other lines [Paα and 1–0 S(3)] have been scaled by the amounts indicated in the figure to match 1–0 S(1) at the centre. The points for all three lines are measured at the same positions, but the Paα points have been shifted 0.5 kpc to the right, and 1–0 S(3) 0.5 kpc to the left for clarity. The bottom panel gives the surface brightness of ionized lines. The ordinate gives the surface brightness of Hα, while Paα has been scaled to match Hα at the centre.

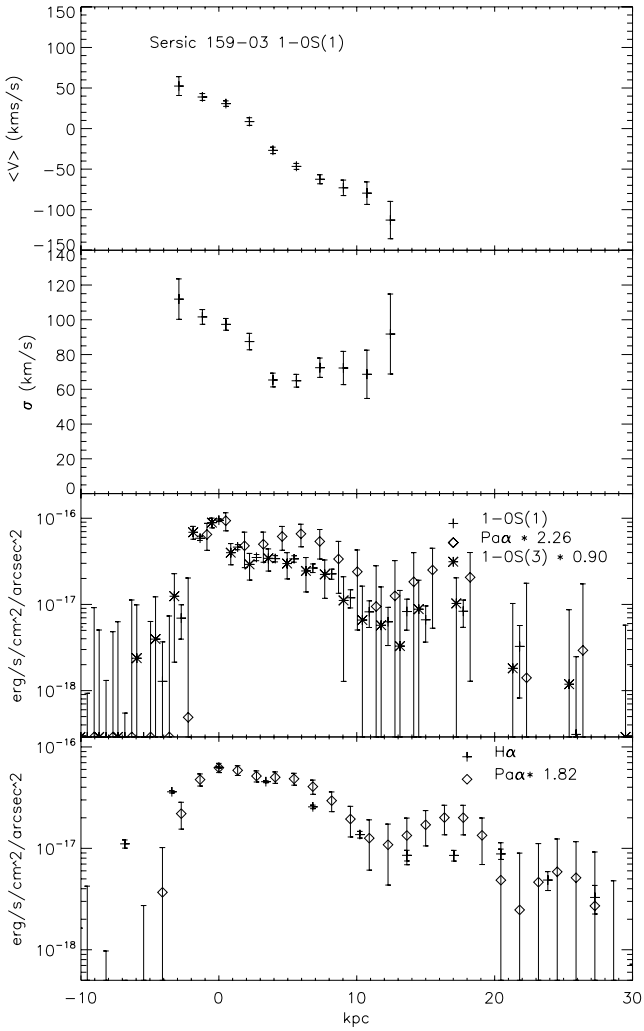

Figure 15. Sersic 159-03 spectral data. The top and second panels give mean velocity and velocity dispersion taken from the 1–0 S(1) line. The third panel gives the IR lines. The ordinate gives the surface brightness of the 1–0 S(1) line, and the other lines have been scaled by the amounts indicated to match 1–0 S(1) at the centre. The points for the various lines have been shifted slightly in the x-direction as described in the previous plot. The bottom panel gives Hα and Paα scaled to match Hα at the centre.

a function of position, showing that these gas phases are closely linked kinematically, even though their dynamical properties, e.g. the ratio of gravitational to drag forces, are quite different because of the large difference in density: $n_e < 10^3\,\mathrm{cm}^{-3}$ in the ionized phase (Heckman et al. 1989) versus $n_e \gtrsim 10^5\,\mathrm{cm}^{-3}$ in the molecular phase (cf. Section 3.2.4). The surface brightness profiles of the atomic and molecular phases also follow broadly similar patterns. In Figs 14(b)–16(b) the brightness profiles integrated across the slit are normalized to the brightest point in the 1–0 S(1) profile. For Abell 2597 the ratio Paα/1–0 S(1) appears a factor of 2 lower at the peak of the profile than in the rest, with molecular and atomic emission otherwise tracing each other. For Abell 2204 the ratio decreases by no more than a factor of 2 from the centre to the edge of the detected nebulosity. For Sersic 159-03 the ratio appears constant across the northern tail, with a decrease of a factor of 2 in the relative strength of Pα at the peak of the profile, similar to that seen in Abell 2597. The current data do not allow us to trace the atomic emission to the south, but the non-detection is consistent with the ratio found for the north.

We have earlier noted (Jaffe et al. 2001) that this ionized/molecular line ratio is relatively constant from cluster to cluster, and is typically at least a factor of 10 lower than that usually seen in photodissociation regions (PDRs) around star-forming regions. The current observations show that this ratio does in fact vary somewhat, by factors of $\sim$2 from cluster to cluster and within clusters. We will discuss in Section 3.3 some of the possible reasons for this variation, but our principal remark is that the excitation sources of the H II and warm H_2 phases must be very closely linked in order that the line ratios and velocities remain so close to each other despite changes in radius by factors >10, in surface brightness by factors >100 and in local velocity dispersion by factors >4.

If we accept the hypothesis that the ratios of H II and H_2 lines are essentially constant over the area where we see H II line emission,

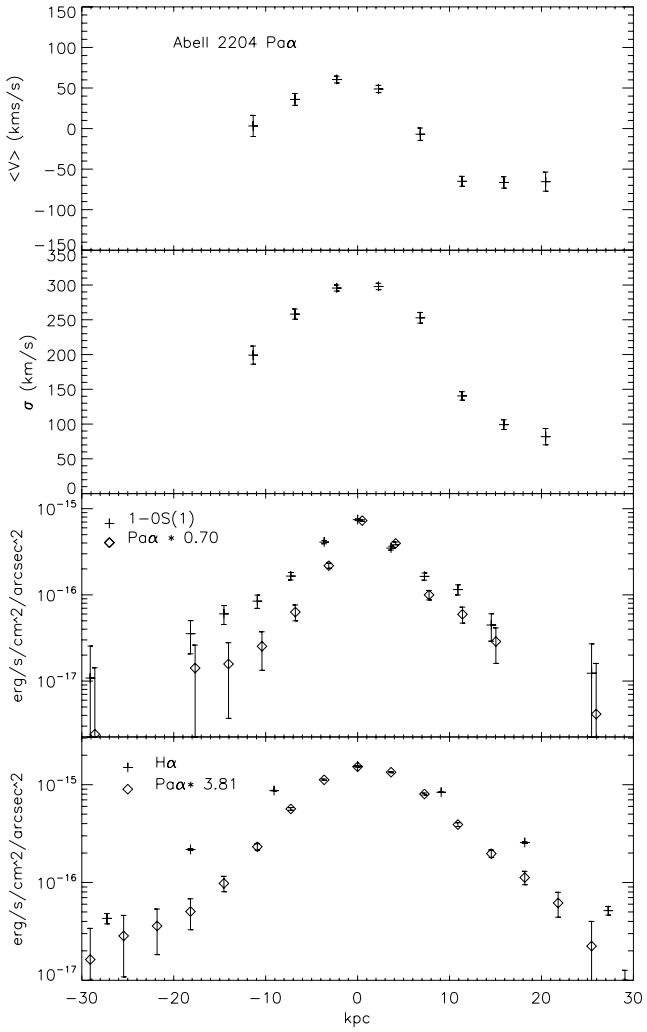

Figure 16. Abell 2204 spectral data. The top and second panels give mean velocity and velocity dispersion taken from the Paα line. The third panel gives 1–0 S(1) and Paα scaled to match 1–0 S(1) at the centre. The bottom panel gives Hα and Paα scaled to match Hα at the centre.

we can calculate total galaxy luminosities in the H_2 lines. As given in Section 3.1, for the 1–0 S(1) line in Abell 2597 this yields $L_1 \sim 2 \times 10^{42}$ erg s^{-1}, for Sersic 159-03 $L_1 \sim 2 \times 10^{41}$ erg s^{-1}, and for Abell 2204 $L_1 \sim 4 \times 10^{41}$ erg s^{-1}, with uncertainties of the order of a factor of 2. The luminosities in the H_2 1–0 S(3) are similar, and detailed models of excitation of H_2 gas in many circumstances (e.g. Black & van Dishoeck 1987; Sternberg & Dalgarno 1989) generally find that the luminosity in the strongest single rotational/vibrational line is generally ∼1–2 per cent of the total molecular NIR emission due to H_2. This implies a typical total H_2 NIR luminosity of 10^{43}–10^{44} erg s^{-1}. This is up to two orders of magnitude greater than the Hα luminosity and may be greater than the total optical line luminosity (assuming that Lyα luminosity is ∼10 times that of Hα).

Kaastra et al. (2004) quote total X-ray fluxes (0.1–2.4 keV) for Sersic 159-03 and Abell 1795 that are approximately 2000 times larger than the Hα fluxes quoted in Table 1. With the conversion factors used in the previous paragraph, the total NIR luminosity for these galaxies is ∼5 per cent of the total X-ray luminosity at all radii, and a larger fraction of that arising in the central ∼20 kpc. For example, in the *Chandra* data of Abell 1795 (Ettori et al. 2002), only about 4 per cent of the total X-ray emission in the 0.5–7 keV range arises in the central 17 kpc. This suggests that the NIR and X-ray luminosities in this central region are similar.

3.2.4 H_2 line ratios and LTE calculations

In Fig. 18 we show the relative strengths of the 1–0 S(1), S(3), S(4) and 2–1 S(3) lines averaged within five spatial regions marked on Fig. 11 and displayed in the form of $\log(F/gA)$ versus $E_{\rm upper}$, where F is the line flux, g the statistical weight of the upper state, A the Einstein coefficient of the upper state, and $E_{\rm upper}$ the energy of the upper state of the transition expressed in temperature units. In LTE, the resulting points should lie on a straight line with slope $1/T_{\rm LTE}$. For Sersic 159-03 the same plots are given in Fig. 19, but the 1–0 S(4) line is not included because its wavelength falls near that of a bright sky line. The values and uncertainties of $T_{\rm LTE}$ printed in each plot are derived solely from the 1–0 S(1) and S(3) lines, which have by far the best signal-to-noise ratios.

Looking first only at the temperature estimates from these two lines, we see in Abell 2597 a gradient of decreasing temperature from the southern region 1 to region 4 at a height of ∼10 kpc. While it is tempting to conclude that the temperature decreases with distance from the nucleus, the estimated average value for the southern region 1 is actually higher than that for region 2. The temperature uncertainty in region 1 is, however, quite large due to the low signal level there. Comparison of the error bounds indicates that, while T_1 could be the same as T_2, it cannot be significantly lower, e.g. not as low as T_3. The weighted best LTE temperature for all five regions together is ∼2600 K, somewhat higher than the central value of 2160 K given by Wilman et al. (2002) for this cluster, but within the range typical for cooling flows. In Sersic 159-03 there is an indication of increasing temperature with distance from the nucleus, but the significance is low. The global average temperature along the slit is ∼2400 K.

In none of the regions is there significant evidence for line ratio deviations from the LTE curve. There are several regions where the signal at the 2–1 S(3) line, which has an excitation energy of 13 890 K, is significant, namely regions 2 and 3 of Abell 2597 and regions 1 and 2 of Sersic 159-03. In these cases the positions of this line near the LTE line imply densities of $n \sim 10^7$ cm^{-3} in order for there to be enough energetic collisions to keep the upper level populated.

3.3 Source of molecular excitation

The problem of the source of excitation of the ionized gas, and to a lesser extent that of the molecular gas, has previously been discussed by many authors, including ourselves. The new contributions of the data reported here consist first of the demonstration of the very close spatial and kinematic correlation of the H II and H_2 lines and secondly of the extension of these correlations to large radii with respect to the central galaxy.

The strong correlation between the emission characteristics of the two gas phases argues that they are excited by a single physical mechanism and not, for example, that stellar photoionization excites the H II region, while heat conduction from the X-ray medium excites the H_2 emission. Shock excitation provides such a natural connection because the various gas phases represent a time sequence in the shock heating and cooling history, but optical spectra in cooling flows at the [O III] λ4363 line (Voit & Donahue 1997 and more stringently Baker 2004) are not consistent with shock models, and we will not discuss these further.

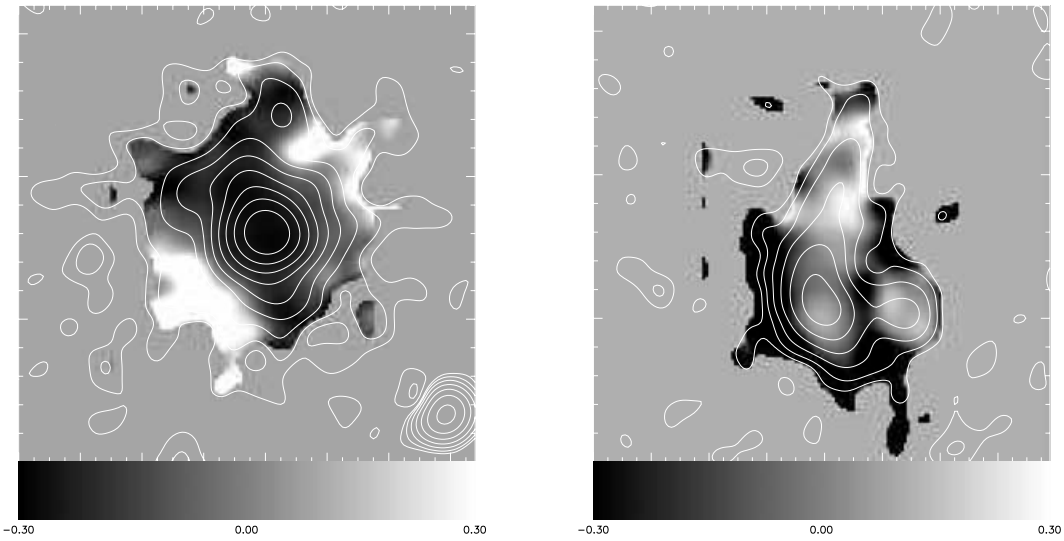

Figure 17. (left) Grey-scale representation of log([N II]/Hα in the central region of Abell 2597 with superimposed contours from Fig. 1. The orientation is the same as Fig. 1, while the field of view covers 60 arcsec in both coordinates. Where the signal-to-noise ratio was low, the grey-scale has been blanked to a uniform grey. (right) Plot of log([N II]/Hα for Sersic 159-03 with the contours from Fig. 2. Again a 60 arcsec field is plotted.

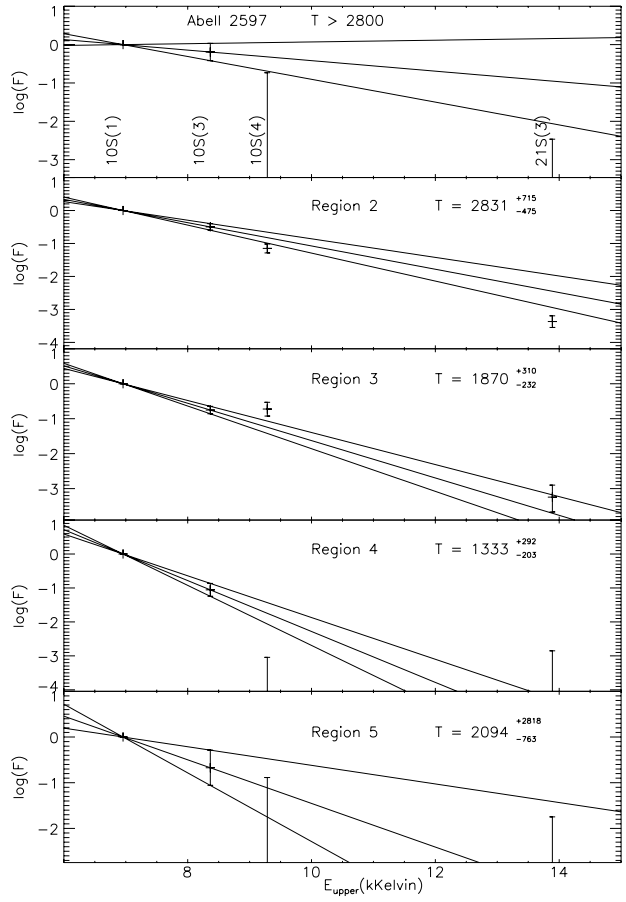

Figure 18. LTE diagrams for Abell 2597. Different regions along the spectrometer slit, marked in Fig. 11, are given in different panels. The abscissa marks the excitation energy of the upper state of each transition (expressed in temperature units), while the ordinate gives the flux of the corresponding line, divided by its Einstein coefficient A and the statistical weight of the upper state g. Finally, each flux is normalized to the flux of the 1–0 S(1) line. In LTE, $F \propto gA \exp(-E_U/kT)$, so the various transitions should lie along a straight line.

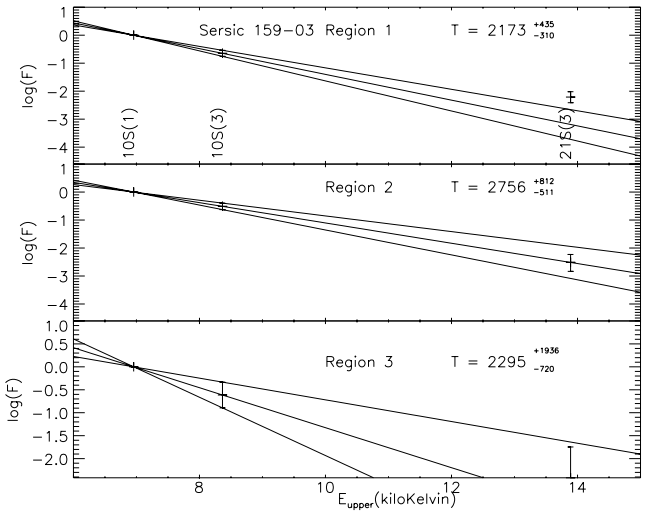

Figure 19. LTE diagrams for Sersic 159-03. The 1–0 S(4) transition lies very close to a sky line at this redshift, and is not given in the plot.

A more likely explanation is excitation of both phases by relatively hard radiation. In star-forming PDRs, excitation by young stars causes H II line emission due to absorption of Lyman continuum photons and subsequent recombination. In these regions, H_2 lines arise from the absorption of Werner and Lyman lines by H_2 at longer wavelengths near 1000 Å and radiative or collisional de-excitation of the molecules (Black & van Dishoeck 1987; Sternberg & Dalgarno 1989). Photons beyond the Lyman limit have a low cross-section for absorption in the H II regions, but can be absorbed in dense H_2 regions with the release of energetic photoelectrons, which lose their energy primarily by spinning up H_2 molecules (Tiné et al. 1997; Maloney, Hollenbach & Tielens 1996). This efficient conversion of hard photons to molecular vibration–rotation lines should lead to higher molecular/ionic line ratios than those from softer sources. In fact, in H_2 regions surrounding planetary nebulae, the molecular/ionic line ratios are similar to those in cooling

flows (Jaffe & Mellema, in preparation). We have not yet carried out detailed modelling of these line ratios in cooling flows, because the large pressure difference between the two phases implies that a full dynamic model, including outflows, is probably necessary.

The assumption of a hard ionizing spectrum is attractive because it is consistent with detailed analyses of the optical spectra (Crawford & Fabian 1992; Voit & Donahue 1997; Baker 2004), which indicate the presence of radiation from a source harder or hotter than O stars (e.g. white dwarfs or Wolf–Rayet stars). O'Dea et al. (2004) find evidence of copious far-ultraviolet (FUV) radiation in the regions of Abell 1795 and 2597 that show molecular emission in our maps, although the radiation detected in the *HST*/STIS observations is not 'hard' compared to the Lyman continuum. The source of these hard photons is still unknown. Crawford & Fabian (1992) suggest, for example, radiation from a non-equilibrium 'mixing layer' of X-ray and molecular gas. Our observations reinforce the need for hard radiation, but do not give direct evidence for its source. They do, however, lead to several interesting constraints on the spectrum and spatial distribution of the exciting photons.

The cooling rate of dense H_2 gas at LTE from rotational/vibrational radiation alone is quite high and the gas is quite difficult to keep warm (e.g. Crawford & Fabian 1992). The cooling rate per molecule from this radiation is about 3×10^{-17} erg s^{-1} near 2000 K. The heating rate is $F_E \sigma_h$, where F_E is the exciting flux (erg s^{-1} cm^{-2}) at energy E, and σ_h is the cross-section for absorbing photons of energy E, which is roughly $\sigma_h \sim 5 \times 10^{-18} (E/20\,\mathrm{eV})^{-3}$ cm^2. If we assume 100 per cent efficiency of converting hard photons to NIR emission, and a uniform distribution of the heating sources within a radius $r \sim 20$ kpc, we can estimate $F_E \sim L_{\mathrm{NIR}}/4\pi r^2$. For $L_{\mathrm{NIR}} \sim 3 \times 10^{43}$ erg s^{-1}, $F_E \sim 10^{-3}$ erg s^{-1} cm^{-2}. Thus even for photons with energies just above 1 Rydberg (say 20 eV), the heating rate per molecule is $\sim 5 \times 10^{-21}$ erg s^{-1} or four orders of magnitude below the cooling rate.

Thus if photons beyond the Lyman limit are the heating source, we must conclude both that these photons are relatively soft – extreme ultraviolet (EUV) rather than soft X-ray – and that the surface filling factor of the photon sources is very low. In other words, the sources of photons must be clumpy and lie very close to the molecular gas, so that the *local* value of F_E is much larger than its *average* value. Because of the difficulty of detecting EUV photons, there is currently little direct evidence for such emission in clusters, and existing observations are limited. Oegerle et al. (2001) detected O VI emission from A2597 in *FUSE* observations, indicating the presence of gas at $\sim 10^5$ K, whereas Lecavelier des Etangs, Gopal-Krishna & Durret (2004) failed to detect the same lines in Abell 1795. Although a *soft excess* of EUV and soft X-rays has now been detected in several clusters (e.g. Kaastra et al. 2003), this is generally detected across the entire cluster, and only in the case of Sersic 159-03 does it show any sign of peaking close to the cluster centre. The large scale of the emission contrasts with the highly clumped nature of any EUV heating source indicated by our data.

The CO observations of Edge (2001) support the idea of clumpy, low surface filling factor, molecular gas; for several clusters the absorbing column calculated from an assumed smooth distribution exceeds that found in X-ray observations. For the clusters Abell 1068 and 1835, for example, Edge (2001) find values of $I_{\mathrm{CO(1-0)}} \equiv \int T_{\mathrm{antenna}}\,\mathrm{d}V$ of approximately 3 and 2 K km s^{-1}, respectively. Israel (1997) shows that the ratio of the column density $N_{\mathrm{H_2}}$ (cm^{-2}) to $I_{\mathrm{CO(1-0)}}$ is typically $\sim 3 \times 10^{21}$ in external galaxies. Thus the CO emission fluxes are equivalent to column densities $N_{\mathrm{H_2}}$ of 9 and 6×10^{21} cm^{-2}. The estimated X-ray *absorption* column densities are, in contrast, about 2×10^{20} for both clusters (Wise, McNamara & Murray 2004; Peterson et al. 2001). The molecular gas implied by the CO observations would have been visible in the X-ray observations had it smoothly covered the regions of X-ray emission; the absence of this absorption implies a small covering factor for the molecular gas.

The luminosity needed to heat the H_2 gas and that missing from the relatively cool gas in cooling flow models (Peterson et al. 2003) are both of the order of $\sim$10 per cent of the total central X-ray flux. This prompts us to speculate that the H_2 medium in fact absorbs and hides most of the softer radiation from the cooling flow. While the X-ray spectra are not consistent with a foreground screen of absorbing gas covering all the emitting gas, they might still be consistent with clumpy selective absorption. Here we postulate that the cooler regions of the X-ray gas, with $T < T_{\mathrm{ambient}}/3$ (Peterson et al. 2003), consist of small clouds each surrounded by even colder, dense, H_2 gas. Because many other processes in the central regions of rich clusters have similar radiative or kinematic luminosities, however, the issue of the H_2 excitation source and/or the heating of the cooler X-ray gas is still wide open.

4 SUMMARY AND CONCLUSIONS

With narrow-band optical imaging of seven clusters, we have shown that Hα and [N II] emission can be traced to beyond 20 kpc from the centre in four clusters previously classified as cooling flows. Although our images of these sources are deeper than those already in the literature, they show very similar morphologies to the previous data. A typical non-cooling flow radio galaxy at a similar redshift to these clusters shows only nuclear Hα emission when observed to the same surface brightness limit.

There are clear variations in Hα morphology from source to source. Two sources are filamentary (Abell 1795, Sersic 159-03) and two are roughly circularly symmetric (Abell 2204, Abell 2597). Abell 2597 shows an azimuthally averaged surface brightness profile, which follows an R^{-3} distribution to beyond 40 kpc (limited by the signal-to-noise ratio in our data). The profiles of the other three clusters drop more rapidly with radius than this. In particular, the filaments in Abell 1795 and Sersic 159-03 appear particularly strongly confined (hence the greater depth of our images show little difference from previously published images). We are therefore seeing a physical limit on the size of the nebulosity, rather than a limit imposed by the signal-to-noise ratio of our images.

Our spectra show that for each source the H_2 emission follows the Paα emission closely in spatial distribution, surface brightness and dynamics across the nebulosity. Clearly all phases of the nebulosity and the source of excitation must be very intimately mixed on scales much smaller than our spatial and spectral resolution. Given the lack of dramatic variation in molecular to atomic emission as a function of radius, the ratio of physical parameters leading to the line ratios varies little over scales of 2–20 kpc from the centre of the cluster. The consequence of this is that we expect to see the molecular gas follow the atomic gas out to well beyond 40 kpc in systems such as Abell 2597. This has a minimal consequence on the total K-band H_2 luminosity because of the rapid drop-off in surface brightness with radius as noted above.

Our detailed and sensitive K-band long-slit spectroscopy of three of these sources confirms the results of Jaffe et al. (2001) that the Paα to H_2 line ratios differ radically from those found in starburst galaxies. They are indicative of excitation and heating by a spectrum harder than O stars (or more particularly a 'bluer' EUV–FUV colour). These data do not allow us to determine whether this is caused by hotter stars, a substantial soft tail to the X-ray spectrum

of the ICM, or some other means. The hardness of the spectrum can be independent of the ionization parameter in the gas.

The difficulty of keeping molecular gas warm by any plausible radiative excitation suggests that in this case the heating sources must be very inhomogeneously distributed, and in close association with the gas clouds. This inhomogeneity of the gas is supported by a comparison of CO emission and X-ray absorption measurements in at least two clusters.

The velocity dispersion curves of the molecular and ionized gas are sharply peaked within 8 kpc of the centres of Abell 2204 and 2597, with dispersions typically peaking at $\sigma \sim 200$–300 km s^{-1}. All previously published *K*-band spectra of cooling flows are of emission from this region. The motions in this region are probably dominated by the energetics of the AGN. In the case of Sersic 159-03, our *K*-band slit traced the large-scale emission filament, did not cross the nucleus of the galaxy and avoids this high velocity dispersion region. Beyond 8 kpc the velocity dispersion drops below the instrumental resolution of approximately 50 km s^{-1}.

The mean velocity of the gas relative to the centres of each system show values of typically ± 100 km s^{-1} and in Abell 2597 and Sersic 159-03 show evidence for coherent shear or rotation over 20–30 kpc. These velocities are much smaller than the typical stellar velocity dispersions in brightest cluster galaxies and are therefore insufficient to support the molecular gas against the gravitational field of the central galaxy. Moreover, the density of the molecular gas indicates that it cannot be pressure-supported in equilibrium with the hot ICM. Either the molecular gas is continually replenished from a pressure-supported reservoir of gas on time-scales of 10 Myr or it is required to be supported by some other mechanism. The kinematics of the molecular gas at large radii seems to exclude an origin for the gas in either material stripped from infalling galaxies or material pushed out of the centre of the system by the action of the central radio source.

ACKNOWLEDGMENTS

The authors wish to thank the Anglo-Australian Observatory and the staff of the Anglo-Australian Telescope, in particular J. Bland-Hawthorn, for their support of the AAT observations. We thank Martin Hardcastle for help with the X-ray data. The ISAAC observations were taken at the Very Large Telescope (VLT) facility of the European Southern Observatory (ESO) as part of Project 71.A-0239. We also thank the ESO staff in Garching and at Cerro Paranal for their support.

REFERENCES

Baker K., 2004, PhD thesis, Univ. Bristol
Black J. H., van Dishoeck E. F., 1987, ApJ, 322, 412
Bland-Hawthorn J., Heath Jones D., 1998, PASA, 15, 44
Böhringer H., 2001, Astron. Gesellschaft Abs. Ser., 18, 122
Crawford C. S., Fabian A. C., 1992, MNRAS, 259, 265
Crawford C. S., Edge A. C., Fabian A. C., Allen S. W., Böhringer H., Ebeling H., McMahon R. G., Voges W., 1995, MNRAS, 274, 75
Crawford C. S., Allen S. W., Ebeling H., Edge A. C., Fabian A. C., 1999, MNRAS, 306, 857
Daines S. J., Fabian A. C., Thomas P. A., 1994, MNRAS, 268, 1060
Donahue M., Mack J., Voit G. M., Sparks W., Elston R., Maloney P. R., 2000, ApJ, 545, 560
Edge A. C., 2001, MNRAS, 328, 762
Ettori S., Fabian A. C., Allen S. W., Johnstone R. M., 2002, MNRAS, 331, 635
Fabian A. C., 1994, ARA&A, 32, 277
Fabian A. C., Mushotzky R. F., Nulsen P. E. J., Peterson J. R., 2001, MNRAS, 321, L20
Falcke H., Rieke M. J., Rieke G. H., Simpson C., Wilson A. S., 1998, ApJ, 494, L155
Hatch N. A., Crawford C. S., Fabian A. C., Johnstone R. M., 2005, MNRAS, 358, 765
Heckman T. M., Baum S. A., van Breugel W. J. M., McCarthy P., 1989, ApJ, 338, 48
Hu E. M., Cowie L. L., Kaaret P., Jenkins E., York D. G., Roesler F. L., 1983, ApJ, 275, L27
Israel F. P., 1997, A&A, 328, 471
Jaffe W., Bremer M. N., 1997, MNRAS, 284, L1
Jaffe W., Bremer M. N., van der Werf P. P., 2001, MNRAS, 324, 443
Kaastra J. S., Lieu R., Tamura T., Paerels F. B. S., den Herder J., 2003, A&A, 397, 445
Kaastra J. S. et al., 2004, A&A, 413, 415
Koekemoer A. M., O'Dea C. P., Sarazin C. L., McNamara B. R., Donahue M., Voit G. M., Baum S. A., Gallimore J. F., 1999, ApJ, 525, 621
Lecavelier des Etangs A., Gopal-Krishna, Durret F., 2004, A&A, 421, 503
McNamara B. R. et al., 2001, ApJ, 562, L194
Maloney P. R., Hollenbach D. J., Tielens A. G. G. M., 1996, ApJ, 466, 561
O'Dea C. P., Baum S. A., Mack J., Koekemoer A. M., 2004, ApJ, 612, 131
Oegerle W. R., Cowie L., Davidsen A., Hu E., Hutchings J., Murphy E., Sembach K., Woodgate B., 2001, ApJ, 560, 187
Osterbrock D. E., 1974, Astrophysics of Gaseous Nebulae. W. H. Freeman, San Francisco
Parker E. N., 1968, ApJ, 154, 49
Peres C. B., Fabian A. C., Edge A. C., Allen S. W., Johnstone R. M., White D. A., 1998, MNRAS, 298, 416
Peterson J. R. et al., 2001, A&A, 365, L104
Peterson J. R., Kahn S. M., Paerels F. B. S., Kaastra J. S., Tamura T., Bleeker J. A. M., Ferrigno C., 2003, ApJ, 590, 207
Sternberg A., Dalgarno A., 1989, ApJ, 338, 197
Taylor G. B., Fabian A. C., Allen S. W., 2002, MNRAS, 334, 769
Tiné S., Lepp S., Gredel R., Dalgarno A., 1997, ApJ, 481, 282
Voit G. M., Donahue M., 1997, ApJ, 452, 242
Wilman R. J., Edge A. C., Johnstone R. M., Crawford C. S., Fabian A. C., 2000, MNRAS, 318, 1232
Wilman R. J., Edge A. C., Johnstone R. M., Fabian A. C., Allen S. W., Crawford C. S., 2002, MNRAS, 337, 63
Wise M. W., McNamara B. R., Murray S. S., 2004, ApJ, 601, 184

This paper has been typeset from a TEX/LATEX file prepared by the author.